NeuroImage 80 (2013) 234–245

Contents lists available at SciVerse ScienceDirect

NeuroImage

journal homepage: www.elsevier.com/locate/ynimg

The Human Connectome Project and beyond: Initial applications of 300 mT/m gradients

Jennifer A. McNab [a,*,1], Brian L. Edlow [b,c,1], Thomas Witzel [c], Susie Y. Huang [c], Himanshu Bhat [d], Keith Heberlein [d], Thorsten Feiweier [e], Kecheng Liu [d], Boris Keil [c], Julien Cohen-Adad [f], M. Dylan Tisdall [c], Rebecca D. Folkerth [g,h], Hannah C. Kinney [h], Lawrence L. Wald [c]

[a] Department of Radiology, Stanford University, R.M. Lucas Center for Imaging, Stanford, CA, USA
[b] Department of Neurology, Massachusetts General Hospital, Boston, MA, USA
[c] Department of Radiology, Massachusetts General Hospital, Athinoula A. Martinos Center for Biomedical Imaging, Boston, MA, USA
[d] Siemens Medical Solutions, USA Inc., USA
[e] Siemens AG, Healthcare Sector, Erlangen, Germany
[f] Department of Electrical Engineering, Ecole Polytechnique de Montreal, Montreal, Quebec, Canada
[g] Department of Pathology, Brigham and Women's Hospital, Harvard Medical School, Boston, MA, USA
[h] Department of Pathology, Children's Hospital Boston, Harvard Medical School, Boston, MA, USA

ARTICLE INFO

Article history:
Accepted 13 May 2013
Available online 24 May 2013

Keywords:
Human connectome
Diffusion MRI
Tractography
Traumatic coma
Consciousness
Axon diameter
Corpus callosum
In vivo
Postmortem

ABSTRACT

The engineering of a 3 T human MRI scanner equipped with 300 mT/m gradients – the strongest gradients ever built for an in vivo human MRI scanner – was a major component of the NIH Blueprint Human Connectome Project (HCP). This effort was motivated by the HCP's goal of mapping, as completely as possible, the macroscopic structural connections of the in vivo healthy, adult human brain using diffusion tractography. Yet, the 300 mT/m gradient system is well suited to many additional types of diffusion measurements. Here, we present three initial applications of the 300 mT/m gradients that fall outside the immediate scope of the HCP. These include: 1) diffusion tractography to study the anatomy of consciousness and the mechanisms of brain recovery following traumatic coma; 2) q-space measurements of axon diameter distributions in the in vivo human brain and 3) postmortem diffusion tractography as an adjunct to standard histopathological analysis. We show that the improved sensitivity and diffusion-resolution provided by the gradients are rapidly enabling human applications of techniques that were previously possible only for in vitro and animal models on small-bore scanners, thereby creating novel opportunities to map the microstructure of the human brain in health and disease.

Introduction

The NIH Blueprint for Neuroscience Research Human Connectome Project (HCP) is in the process of mapping the connections of the adult human brain as completely as possible using diffusion tractography, functional MRI (FMRI), magnetoencephalography (MEG), electroencephalography (EEG) and genetics. This comprehensive initiative involves two different consortia: the Washington University, the University of Minnesota and Oxford University consortium (WU–Minn HCP) and the Massachusetts General Hospital and the University of California, Los Angeles consortium (MGH–UCLA HCP). The "connectome" map will integrate complementary efforts from both HCP consortia and provide a new foundation for understanding neural network connectivity and structural neuroanatomy. In addition to its basic neuroscience merits, mapping of healthy adult human connectomes provides a basis for studying how connectomes change as humans learn, mature and age, and how a connectome becomes dysfunctional with injury or disease.

Beyond these high impact scientific contributions, the legacy of the HCP will also include its significant technological advancements. Prominent among these are MRI scanners equipped with significantly stronger magnetic gradients. The WU–Minn HCP involves a human 3 T MRI with 100 mT/m maximum gradients (Van Essen et al., 2012). The MGH–UCLA HCP involves the first ever human MRI scanner equipped with 300 mT/m gradients (7.5× stronger than the clinical standard (40 mT/m)) and a 64-channel phased-array receiver coil (Keil et al., 2012). This MRI technology, which was engineered specifically for the HCP, has already been applied to several additional in vivo neuroimaging studies, which are impractical or underserved by

* Corresponding author. Fax: +1 650 723 9222.
E-mail address: mcnabj@stanford.edu (J.A. McNab).
[1] Jennifer A. McNab and Brian L. Edlow are co-first authors of this manuscript.

1053-8119/$ – see front matter © 2013 Elsevier Inc. All rights reserved.
http://dx.doi.org/10.1016/j.neuroimage.2013.05.074

existing technology. A detailed description of the novel hardware employed by the MGH-UCLA consortia and a characterization of the improvements in data quality provided by this hardware can found in Setsompop et al. (2013). Here we describe how the 300 mT/m gradients of the MGH–UCLA connectome scanner are creating new ways to probe the human brain and opening up new possibilities to serially investigate changes in brain tissue microstructure. This paper focuses on the first imaging studies conducted on the MGH–UCLA connectome scanner that fall outside the immediate scope of the HCP but are an impactful byproduct of its technological developments. Namely, we present initial results for: diffusion tractography of the pathways that mediate human consciousness and recovery after traumatic coma, in vivo mapping of axon diameter distributions and postmortem diffusion imaging.

There are two key advantages provided by an MRI scanner with 7.5× stronger magnetic gradients, both of which have been instrumental in facilitating the neuroimaging applications discussed here. First, the stronger gradient amplitudes achieve a given diffusion-encoding gradient area in less time. This reduces the entire diffusion-encoding period and the echo time. As a result, the T_2 decay is reduced and the signal-to-noise ratio (SNR) is increased. Second, the larger gradient amplitudes enable "stronger" diffusion encoding (larger diffusion-encoding gradient areas, larger q-values and b-values) to be achieved in practical times. The resulting enhancement in the "diffusion resolution" represents a smaller spatial scale at which differences in spin displacements can be resolved. Together, these advantages of stronger magnetic field gradients dramatically increase the sensitivity to tissues with short T_2 and improve q-space diffusion imaging methods that demand large diffusion-gradient areas.

q-Space diffusion imaging

q-Space diffusion imaging (Callaghan, 1991; Cory and Garroway, 1990) samples multiple q-values, where a q-value is proportional to the diffusion-encoding gradient area. The Fourier Transform of the signal attenuation at multiple q-values describes the diffusion propagator, i.e. the probability density function (PDF) that a particle has been displaced a specific distance along a given orientation during a given diffusion time. The maximum q-value determines the diffusion resolution and hence the stronger connectome gradients probe sharper features of the diffusion PDF in less time and with less T_2 loss, thereby pushing q-space imaging methods beyond prior capabilities. The stronger connectome gradients also allow a given q-value to be reached in a shorter diffusion time, probing the barriers experienced by the diffusing water molecules on a short time scale.

In this work we use a novel gradient system, 300 mT/m, slew-rate 200 T/m/s (Siemens AS302), integrated into a clinical 3 T MRI scanner (MAGNETOM Skyra CONNECTOM, Siemens Healthcare). We use these capabilities to explore a broader q and diffusion time (Δ) parameter space than was previously possible in humans in vivo. Here, we show that beyond mapping of the human connectome, there are a number of additional applications of the connectome's gradients that are rapidly advancing our ability to probe the structural basis of human brain function.

Diffusion spectrum imaging of traumatic coma recovery

Traumatic coma affects more than 1 million people worldwide each year (Bruns and Hauser, 2003; Faul et al., 2010). In addition, hundreds of military personnel have experienced a severe traumatic brain injury (TBI) causing coma since the start of the wars in Afghanistan and Iraq (Bell et al., 2009; DuBose et al., 2011). For these civilians and military personnel with traumatic coma, recovery of consciousness requires the activation and integration of brain networks that support the two critical components of consciousness: arousal (wakefulness) and awareness (Kinney and Samuels, 1994). Advanced neuroimaging techniques have begun to identify the neural networks in the cerebral hemispheres that enable recovery of awareness (Fernandez-Espejo et al., 2012; Vanhaudenhuyse et al., 2010), but the pathways in the brainstem ascending reticular activating system (ARAS) that facilitate recovery of arousal after coma have yet to be elucidated. Since the discovery of the ARAS by Moruzzi and Magoun in 1949 (Moruzzi and Magoun, 1949), the vast majority of ARAS connectivity studies have been performed in animal models (Fuller et al., 2011; Gennarelli et al., 1982; Smith et al., 2000), with human studies mostly being limited to two-dimensional lesion mapping analyses (Parvizi and Damasio, 2003) and functional activation studies using positron emission tomography (Kinomura et al., 1996; Silva et al., 2010).

Diffusion tractography is a promising tool for elucidating the structural connectivity of ARAS pathways in the human brainstem. One of the principal challenges, however, is detecting the crossing fibers that are a prominent component of the ARAS network (Nauta and Kuypers, 1958). Diffusion Spectrum Imaging (DSI) (Callaghan et al., 1988; Wedeen et al., 2005) is one of several diffusion techniques that provides a means of detecting these crossing fibers. DSI requires the acquisition of multiple q-values and diffusion orientations arranged in a lattice in q-space (q_x,q_y,q_z). A 3D Fourier transform of this q-space lattice yields the 3D spin displacement PDF. The orientation distribution function (ODF) along a given orientation is then the radial projection of the spin-displacement PDF. Maxima on the ODF are used to identify fiber orientations.

Here, we analyze ARAS connectivity with deterministic tractography on DSI ODFs and probabilistic tractography on the ball and two stick model using the connectome scanner's 300 mT/m gradients in a 27-year-old man who recovered from traumatic coma. Six years and seven months prior to being imaged on the MGH-UCLA connectome scanner, the patient had experienced a severe TBI caused by a car that hit him while he was riding his bike. He was in a coma for 14 days, and a clinical MRI scan performed on day 7 post-injury revealed multiple microhemorrhages in the cerebral hemispheres, splenium of the corpus callosum, and brainstem (bilaterally), consistent with severe grade 3 diffuse axonal injury (Adams et al., 1989). After emergence from coma, the patient underwent one and a half months of inpatient rehabilitation, followed by one year of outpatient rehabilitation. By the time of his MGH–UCLA connectome scan, the patient's Glasgow Outcome Scale—Extended score was 7 (out of a maximal score of 8), indicating "good recovery," and his Disability Rating Scale score was 0, indicating that he was completely independent with activities of daily living and had returned to a normal work environment — one of few patients with bilateral traumatic axonal injury lesions in the brainstem who has been reported to experience this level of recovery (Skandsen et al., 2011).

Axon diameter mapping

A different genre of q-space imaging focuses on sampling temporal q-space rather than spatial q-space (i.e. acquiring multiple q-values at multiple diffusion times). If sufficiently high q-values and a sufficiently wide range of diffusion times are acquired, it is possible to extract information about the size of restricted compartments, such as axons, based on theoretical models of the diffusion diffraction patterns that they will generate.

The diameter of an axon is proportional to the speed at which action potentials are conducted along its length (Hoffmeister et al., 1991; Hursh, 1939). Therefore, any change in the distribution of axon diameters in a white matter tract can putatively impact the operation of neural networks (Ringo et al., 1994). Axon diameter has also been linked to several neurological disorders. For example, large diameter axons are thought to be selectively damaged in amyotrophic lateral sclerosis patients (Cluskey and

Ramsden, 2001; Heads et al., 1991). Smaller diameter axons are thought to be maldeveloped in autistic children (Piven et al., 1997). Smaller diameter axons are also thought to be the most vulnerable to neurodegeneration associated with aging (Marner et al., 2003).

The majority of axon diameter mapping using MRI has been performed in vitro (Assaf et al., 2008; Ong and Wehrli, 2010; Stanisz et al., 1997) and in animal models (Barazany et al., 2009) due to the demands for strong encoding gradients which have, thus far, only been available on small bore MRI scanners. Despite this, at least one group has now demonstrated estimation of an axon diameter index, a′, in the in vivo human brain using a standard clinical gradient strength of 40–60 mT/m (Alexander et al., 2010; Zhang et al., 2011). The ActiveAx (a′ contrast) and the AxCaliber technique developed by Assaf et al. (2008) are very similar. The output for ActiveAx provides a single statistic of the axon diameter distribution (the weighted mean) whereas AxCaliber estimates the mean and variance of the gamma distribution estimated by AxCaliber. ActiveAx is also orientationally invariant whereas the canonical version of AxCaliber is not. Therefore, ActiveAx shows significant promise for rapid clinical translation of axon diameter estimates. The sensitivity of both methods is limited by the SNR and range of achievable q-values and diffusion times, and these factors are directly linked to the maximum available gradient strength. AxCaliber has also recently been demonstrated in vivo at 40 mT/m maximum gradient strengths (Horowitz et al., 2012). Although the data presented here do not represent the first attempt at axon diameter mapping in the in vivo human brain, they are the first AxCaliber in vivo human data acquired with a similar gradient strength (G_{max} = 300 mT/m) to the animal studies used to validate the methodology (Barazany et al., 2009).

While AxCaliber has previously been applied in the in vivo human brain using 40 mT/m gradients (Horowitz et al., 2012), here we present the first ever in vivo human brain AxCaliber data using 300 mT/m gradients. We focus on the corpus callosum because of the availability of gold standard electron microscopy in this region and because of the critical role that inter-hemispheric trans-callosal connections play in many cognitive functions.

High-resolution (0.6 mm isotropic) q-ball imaging in fixed human brain

Diffusion imaging of whole, fixed human brains has gained traction in recent years as a method of obtaining a type of gold-standard, high-spatial resolution, high-SNR data without the motion artifacts or distortions that constrain in vivo acquisitions. Postmortem diffusion images also provide a useful link between in vivo imaging and histology. Postmortem scans allow us to see what additional microstructural information we might be able to visualize if/when we are able to improve the sensitivity and image fidelity of in vivo acquisitions. For example, diffusion anisotropy in the cerebral cortex was first identified in postmortem diffusion imaging (Leuze et al., 2012; McNab et al., 2009; Miller et al., 2011) and has now, with the improved resolution of in vivo diffusion imaging, been identified in vivo by several groups (Anwander et al., 2010; Heidemann et al., 2010; McNab et al., 2013).

While postmortem diffusion imaging of whole, fixed human brains benefits from long scan times and the absence of motion, it is hindered by decreased T_2 relaxation times (due to the fixation process) (D'Arceuil et al., 2007; McNab et al., 2009) and reduced apparent diffusion coefficients (ADCs). Each of these limitations puts competing demands on the diffusion sensitization. Specifically, the diffusion sensitization must be both stronger and executed in less time. As such the gradients of the MGH–UCLA connectome scanner have the potential to dramatically improve the quality of diffusion imaging in whole, fixed, human brain specimens.

Methods

All data were acquired using the MGH–UCLA connectome scanner which consists of a novel AS302 gradient system that is part of a new 3 T system (MAGNETOM Skyra CONNECTOM, Siemens Healthcare) capable of up to 300 mT/m and a slew rate of 200 T/m/s. The slew rate was de-rated to 62.5 T/m/s during the diffusion encoding to prevent physiological stimulation. A custom-made 64-channel phased array coil was used for signal reception (Keil et al., 2012). All studies were performed with the approval of the institutional review board. Written consent was obtained from subjects for the in vivo studies and from family surrogate decision-makers for the ex vivo studies.

Diffusion spectrum imaging of traumatic coma recovery

ARAS connectivity was assessed in the 27-year-old patient and in four age-matched healthy control subjects (2 men, 2 women; average age 25.8, age range 23–29) using a DSI protocol with a 515 q-space lattice. Images with b = 0 s/mm^2 were interspersed every 16 images (39 in total) and positive and negative gradient pairs from the q-space lattice were acquired sequentially. The protocol parameters were b_{max} = 10,000 s/mm^2, gradient pulse duration (δ) = 12.9 ms, diffusion time (Δ) = 20.9 ms, TE/TR = 47/5900 ms, FOV = 22 cm × 22 cm, 80 slices, 2 mm isotropic voxels, partial Fourier = 6/8, parallel imaging using generalized autocalibrating partially parallel acquisitions (GRAPPA) with an acceleration factor R = 3, BW = 2526 Hz/pixel, echo spacing = 0.53 ms, and acquisition time = 55 min.

Image registration of the interspersed b = 0 images was used to correct for bulk motion between scans using FLIRT (www.fmrib.ox.ac.uk/fsl). Correction of eddy-current induced distortions was achieved using opposite polarity DWI pairs (Bodammer et al., 2004), which were registered one to the other, constraining for the expected translations, dilations and shears. The half-way transform was then calculated and applied. Motion correction and eddy current correction transformations were applied in a single step to prevent further blurring.

For the tractography analysis, we focused on the pedunculopontine nucleus (PPN), which is a major source of cholinergic innervation to the thalamic intralaminar and reticular nuclei, and thus a principal component of the ARAS arousal network (Edlow et al., 2012; Parvizi and Damasio, 2001; Reese et al., 1995). The PPN was chosen because this arousal nucleus was affected unilaterally by a focus of hemorrhagic axonal injury that was identified on both the acute (i.e. day 7) gradient-recalled echo sequence and the susceptibility-weighted imaging sequence acquired on the MGH–UCLA connectome scanner (Fig. 1a). For the patient and the four controls, the PPN was manually traced on the diffusion-weighted images at the level of the caudal midbrain, and the thalamic intralaminar nuclei (centromedian/parafascicular [CEM/Pf] and central lateral [CL]) and reticular (Ret) nuclei were traced at the level of the mid-thalamus in accordance with standard neuroanatomic atlases (Fig. 1b) (Mai et al., 2008; Paxinos et al., 2011). Diffusion data were processed for both deterministic and probabilistic tractography. Deterministic tractography analysis was performed using the Diffusion Toolkit and TrackVis (www.trackvis.org) (Wang et al., 2007) and the probabilistic tractography was performed using the FMRIB Software Library (FSL) (www.fmrib.ox.ac.uk/fsl) (Behrens et al., 2003). For the deterministic tractography, TrackVis employs a Gaussian filter with a roll-off of 0.5 at the edge of q-space before reconstructing ODF and no peak threshold nor limit to the maximum orientations per voxel was employed (Wedeen et al., 2008). For the probabilistic tractography the ball and two stick model implemented in FSL was used. We did not use the multi-shell model implemented by Jbabdi et al. (2012). Our probabilistic tractography results are potentially confounded by the effects of overfitting and should be interpreted as such. We chose to perform both deterministic and probabilistic

tractography analyses because we found it helpful to use the visualization tools available in TrackVis but also wanted to provide a quantitative comparison between the different pathways in different subjects.

In order to quantitatively compare the probabilistic tractography results we report what we will refer to as the "probabilistic streamline connectivity index" (PSCI), which we define as: [total number of streamlines reaching the target mask] / [the total number of streamlines propagated from seed mask] / [the total number of voxels in seed region + the total number of voxels in target region]. Five thousand streamlines were propagated from each voxel within the PPN seed region. Probabilistic tractography suffers from a "flare" of high streamline probability near the seed ROI compared to more distant locations. We therefore used the distance correction option (−pd) implemented in FSL's probtrackx (www.fmrib.ox.ac.uk/fsl). With this option, the connectivity distribution at each voxel equals the average length of the pathways that cross the voxel multiplied by the number of samples that cross it. The distance correction was applied because the distances between the seed region of interest (PPN) and the target regions of interest (CEM/Pf, CL and Ret) are different, and we did not want our PSCI measurements to be biased by distance. Using Figure 27 from Morel's atlas (Morel et al., 1997) we estimated the distance from the inferior margin of the red nucleus (which represents the superior margin of the PPN seed region used in our analysis), to the superior margin of each thalamic target nucleus. Taking into account the 1.0 mm-to-2.8 mm scaling factor in the atlas, we estimate distances of 12.6 mm for PPN-to-CEM/Pf, 25.2 mm for PPN-to-CL, and 28.0 mm for PPN-to-Ret. Lastly, a loop-check was applied to prevent streamlines from looping back on themselves.

Axon diameter mapping in the in vivo human brain

Four volunteers (2 male, 2 female, age range 23–48) were scanned. The experimental protocol, which follows closely from Barazany et al.'s rat imaging protocol, consisted of a series of sagittal 2 mm isotropic resolution diffusion-weighted-stimulated echo-echo planar imaging (DW-STE-EPI) acquisitions with 17 contiguous sagittal slices centered on the midline of the corpus callosum with TE/TR = 54/3100 ms, parallel imaging using GRAPPA with an acceleration factor R = 2, δ = 8.7 ms, 17 diffusion gradient increments (25–241 mT/m), and 12 averages. The maximal b-value (at the longest diffusion time) was 10,000 s/mm^2. The diffusion gradients were applied along the z-direction (perpendicular to the fibers of the corpus callosum) in the mid-sagittal plane. The experiment was repeated for five different diffusion times: 35, 44, 54, 84 and 120 ms. Total acquisition time was 53 min. Motion and eddy-current correction were applied in the same manner as described for the DSI data. The AxCaliber (Assaf et al., 2008) method was used to estimate axon diameter distributions within hand-drawn ROIs in a single slice in the mid-sagittal plane in the splenium, body and genu of the corpus callosum. Note that we did not use a CSF compartment in our signal model, as was done by Barazany et al. (2009).

The AxCaliber method is a parametric fit of a close-form model to our data. The AxCaliber model was fit simultaneously to all data points at all diffusion times using in-house Matlab (MathWorks, Natick, MA) code that employs a nonlinear least-square routine (utilizing Levenberg–Marquardt minimization). Following previous demonstrations of the AxCaliber method in in vivo rat brain (Barazany et al., 2009), the diffusion coefficient of the restricted component was fixed to 1.4 μm^2/ms. Therefore, we fit for the 4 parameters used in the AxCaliber model: the hindered diffusion fraction (fh), the hindered diffusion coefficient (Dh) and α and β parameters that describe the gamma function used to model the distribution of different axon diameters. Note that we modeled only two components and therefore the restricted fraction (fr) is equal to 1-fh. The optimization was constrained with initial conditions/lower bounds/upper bounds set to: fh = 0.5/0.0/1.0, Dh = 1/0.01/100 μm^2/ms, α = 12/2/50,

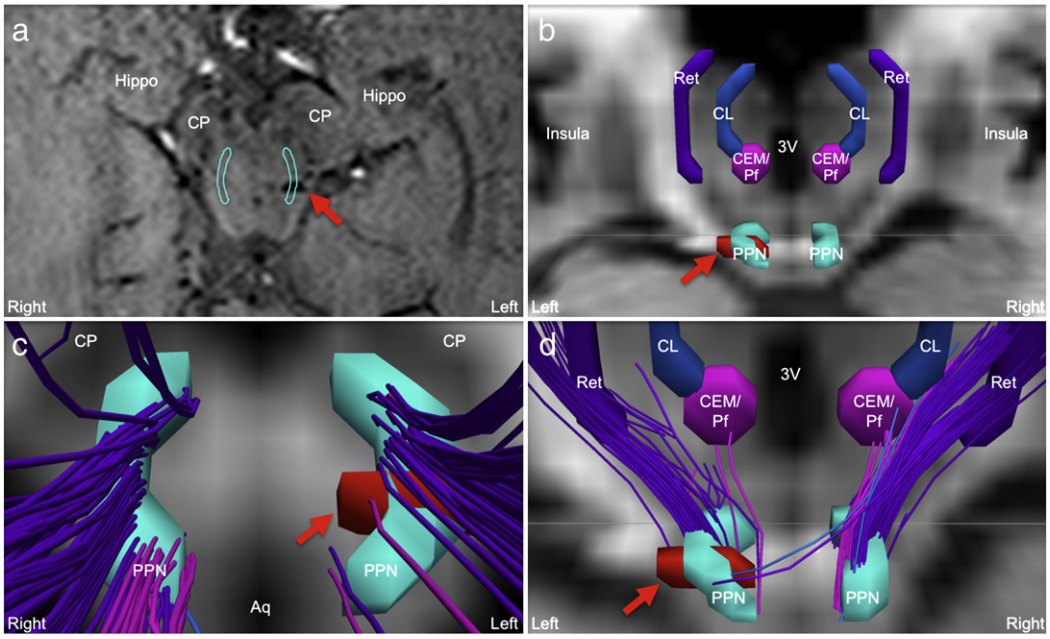

Fig. 1. Regions of interest and deterministic tractography results for ARAS connectivity analysis in a patient who recovered from traumatic coma. a) Zoomed axial view of a susceptibility-weighted image at the level of the traumatic microhemorrhage (red arrow) in the dorsolateral midbrain. The hemorrhage is seen overlapping with the left pedunculopontine nucleus (PPN) at this level (turquoise outlines). b) Posterior view of regions of interest (ROIs) for the PPN (turquoise), and the thalamic target nuclei: centromedian/parafascicular nucleus (CEM/Pf, pink), central lateral nucleus (CL, blue) and the reticular nucleus (Ret, purple). All ROIs are superimposed on an axial diffusion-weighted image (DWI) at the level of the caudal midbrain and a coronal DWI at the level of the mid-thalamus. The microhemorrhage shown in panel a) is color-coded red and indicated by the red arrow. This hemorrhage involves the dorsal aspect of the left PPN nucleus. c) Inferior view of deterministic streamlines passing through the PPN at the level of the caudal midbrain. Streamlines are color-coded according to the thalamic nucleus with which they connect: pink, PPN-CEM/Pf; blue, PPN-CL; purple, PPN-Ret. The microhemorrhage is again shown in red and indicated by the red arrow. d) Zoomed posterior view from panel b) demonstrating streamlines connecting PPN to CEM/Pf, CL, and Ret. The hemorrhage is indicated by the red arrow. In panels c) and d), fewer streamlines are seen passing through the left PPN, particularly in the region of the hemorrhage, as compared to the right PPN. Neuroanatomic landmarks: 3V, third ventricle; Aq, cerebral aqueduct; CP, cerebral peduncle; Hippo, hippocampus.

$\beta = 0.4/0.1/10$. The upper and lower bounds of axon diameters used in the fit were: $0 < a < 50$ μm.

High-resolution (0.6 mm isotropic) q-ball imaging in fixed human brain

One whole, fixed human brain from a 58-year-old woman who died of non-neurological causes was scanned on the MGH–UCLA connectome scanner. The excised brain was placed in fixative (10% formaldehyde) after a 14 hour postmortem interval. It remained in fixative for 7 months prior to scanning on the MGH–UCLA connectome scanner. At the time of scanning, the brain specimen was transferred from the fixative solution to a Fomblin solution (perfluoropolyether, Ausimont USA Inc., Thorofare, NJ) to prevent bright protonated fluid signal surrounding the specimen from reducing the dynamic range within the tissue signal values of interest. We used a 3D segmented-EPI diffusion-weighted spin echo pulse sequence, which is the same as has been used previously for postmortem diffusion imaging (Miller et al., 2011) except that here we used a single refocusing pulse and mono-polar gradients rather than a twice-refocused spin-echo. The protocol parameters were 0.6 mm isotropic voxels, 44 diffusion-encoding orientations at a b-value of 10,000 s/mm^2, $\delta = 13.5$ ms, $\Delta = 26.8$ ms, 5 b = 0 s/mm^2 images, TE/TR = 59/750 ms, FOV = 180 mm × 174 mm, slab thickness = 176 mm, matrix = 296 × 288 × 288, partial Fourier = 6/8, BW = 995 Hz/pixel, and echo train length = 32. The total acquisition time was 26.5 h (32.4 min per volume).

We compare the whole, fixed brain data with data previously acquired (Edlow et al., 2012) on a dissected brainstem–diencephalon specimen (consisting of pons, midbrain, thalamus, hypothalamus, and basal forebrain) from a 53-year-old woman who died of non-neurological causes. These data were acquired with a 3D diffusion-weighted spin echo echo-planar imaging sequence with 60 diffusion-encoding orientations, b = 4057 s/mm^2 and a maximum gradient strength of 124 mT/m, diffusion gradient duration = 13.4 ms, diffusion time = 25 ms, TE/TR = 72.5/1000 ms, FOV = 7.2 × 7.2 × 8.2 cm, and matrix = 128 × 128 × 128. One b = 0 s/mm^2 image was also acquired for a total acquisition time of 2 h 10 min.

Voxel-wise ODFs were reconstructed for the whole, fixed brain data acquired on the MGH–UCLA connectome scanner using Diffusion Toolkit software (Wang et al., 2007), which employs the spherical harmonic basis method (Hess et al., 2006). Within each axial slice, we selected regions of interest (5 × 5 voxels each) that are known to contain a high concentration of crossing fibers, and then tested the ability of connectome's 300 mT/m gradients to detect intravoxel crossing fibers with ODFs in the ex vivo human brainstem. For the midbrain region of interest, we chose the cuneiform/subcuneiform nucleus (i.e. mesencephalic reticular formation), which has been shown in animal (Kaufman and Rosenquist, 1985; Nauta and Kuypers, 1958; Shute and Lewis, 1963; Steriade and Glenn, 1982; Vertes and Martin, 1988) and human (Edlow et al., 2012) studies to contain a complex meshwork of crossing fibers that project ventrally to the hypothalamus, superiorly to the thalamus, and laterally to the contralateral midbrain tegmentum. For the pontine slice, we chose the paramedian region of the basis pontis, which is well known to contain pontocerebellar fibers traveling in the medial–lateral plane and corticospinal tract fibers traveling in the superior–inferior plane.

Results

Diffusion spectrum imaging of traumatic coma recovery

In both the deterministic and the probabilistic analyses, streamlines were identified between the PPN and the CEM/Pf, CL, and Ret in all four control subjects, consistent with a recent deterministic tractography analysis of ARAS connectivity in the ex vivo and in vivo human brain (Edlow et al., 2012). For the four controls, PSCI values (mean +/− SD) for PPN-CEM/Pf, PPN-CL, and PPN-Ret, were 0.026 +/− 0.006, 0.032 +/− 0.02, and 0.066 +/− 0.01, respectively. For the patient, streamlines were also identified in both the deterministic and probabilistic analyses between the PPN and each group of thalamic nuclei. In the quantitative probabilistic tractography analysis, PSCI values were 0.016 for PPN-CEM/Pf, 0.016 for PPN-CL, and 0.050 for PPN-Ret (Fig. 2). When ranking PSCI values for the patient and the control subjects, the patient's PSCI values ranked the lowest for PPN-CEM/Pf (0.016 vs. control range 0.019 to 0.034), the second lowest for PPN-CL (0.016 vs. control range 0.015 to 0.057), and the lowest for PPN-Ret (0.050 vs. control range 0.053 to 0.070).

Since one of the patient's traumatic hemorrhages involved part of the left PPN (Fig. 1d), an analysis was performed to assess for differences in left-versus-right-sided PPN connectivity between the controls and the patient. A comparison of PSCI values in the left and right sides of the brainstem-diencephalon for the PPN-CEM/Pf, PPN-CL and PPN-Ret pathways is shown in Fig. 3. Using a one-sample t-test in MATLAB, we tested the null hypothesis that the absolute difference between the left and right PSCI values in the patient was the same as the mean of the absolute difference between the left and right PSCI values in the four controls. For the PPN-CEM/Pf and PPN-CL pathways the null hypothesis was not rejected indicating that there was no evidence of a significant difference between the controls and the patient. However, for the PPN-Ret pathway, the null hypothesis was rejected with a p-value =0.001 and a confidence interval between −0.0014 and 0.0119, indicating a potential significant laterality difference between the controls and the patient for the PPN-Ret pathway.

Axon diameter mapping in the in vivo human brain

Fig. 4 shows an example of the data quality (12 averages per image and echo times matched across b-values) used for the AxCaliber analysis. The in vivo human q-space diffusion MRI estimates of axon diameter distributions using the MGH–UCLA connectome scanner are in good correspondence with literature. The histological analysis of Aboitiz et al. (1992) suggests that thin fibers are most dense in the genu, less dense posteriorly towards the posterior midbody where they reach a minimum, and then denser again towards the splenium. Aboitiz et al. report that large fibers have a pattern complementary to that of thin fibers with a peak in density in the posterior mid-body. Aboitiz et al. also provide some evidence that the distribution of axon diameters is broader in the body compared to the genu and splenium, with one subject exhibiting distributions of 0.5–8.5 μm for the body, 0.5–3.5 μm for the genu, and 0.5–5 μm for the splenium.

In our group analysis, the estimated axon diameter distributions for the genu and splenium are centered at 0.5 μm and 0.9 μm, respectively, and the body of the corpus callosum is not only shifted to larger axon diameters with a distribution centered at 7.7 μm but it also has a broader distribution representing a wider range of axon diameters (Fig. 5d). This trend is largely consistent between the 4 subjects with the exception that subject 3 shows a broader distribution for the genu that is also shifted to axon diameters of approximately 3 μm (Fig. 6). Pixel-wise analysis also provides clear evidence of the difference in axon diameters in the genu and splenium relative to the body (Figs. 7a–d). Axonal density maps (Figs. 7e–h) show some evidence of higher axonal density in the splenium and the genu but generally more uniformity anterior to posterior.

High-resolution (0.6 mm isotropic) q-ball imaging in fixed human brain

The 3D segmented-EPI read-out utilized for the whole-brain ex vivo scan greatly reduces distortions compared to the standard single-shot methods used in vivo. Evidence of this image fidelity is readily apparent in Fig. 8d. Qualitatively we also see an impressively detailed delineation of the cerebellar-pontine crossing fibers in Fig. 8f. While the data on the brainstem-diencephalon specimen (Figs. 8c and

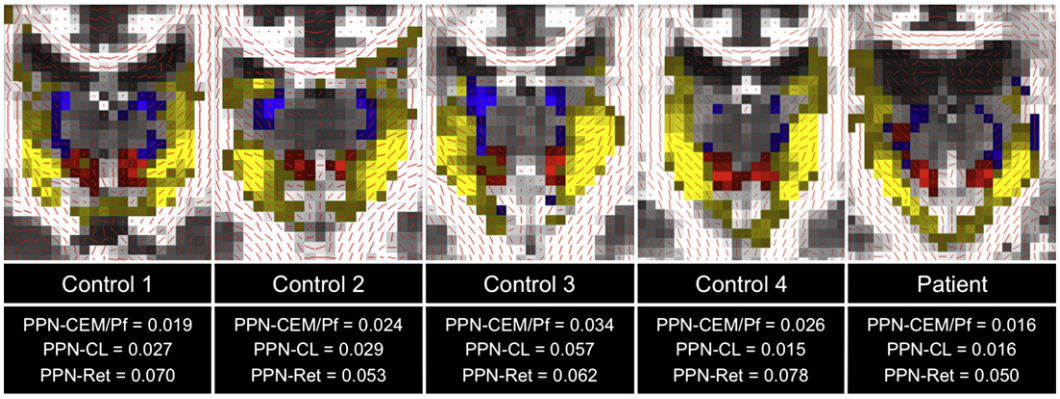

Fig. 2. Probabilistic tractography results for the four control subjects and the patient who recovered from traumatic coma. Probabilistic data are superimposed on a coronal grayscale fractional anisotropy map at the level of the mid-thalamus. Within each voxel, the primary diffusion vector is shown in red: medial–lateral vectors are seen in the body of the corpus callosum at the superior margin of each image, and superior–inferior vectors are seen in the posterior limbs of the internal capsules at the lateral margins of each image. Probabilistic data for each analysis of pedunculopontine nucleus (PPN) connectivity are color-coded according to the thalamic nucleus with which the streamlines are connecting: red, centromedian/parafascicular nucleus; blue, central lateral nucleus; yellow, reticular nucleus. The intensity of the color in each voxel represents the number of streamlines passing through that voxel (i.e. brighter voxels represent a higher streamline count than darker voxels). For the purpose of clarity and to exclude streamlines with low probability, streamline results are thresholded in each analysis to show voxels with between 1000 and 10,000 streamlines passing through them.

e) provides a similar level of detail, a whole human brain does not fit in the small-bore 4.7 T scanner and without whole-brain data it is impossible to assess structural connectivity between the brainstem and the cerebral hemispheres.

ODF analyses of directional water diffusion within the cuneiform/subcuneiform nucleus (Fig. 9) and basis pontis (Fig. 10) revealed that the 300 mT/m gradients of the connectome scanner can detect multidirectional water diffusion in the ex vivo human brain at a high spatial resolution (0.6 mm isotropic voxels). Within the cuneiform/subcuneiform nucleus, at least three distinct vectors of water diffusion project in the superior–inferior, medial–lateral, and anterior–posterior planes, respectively. Similarly, within the basis pontis, the ODFs resolve intravoxel crossing fibers of multiple white matter pathways.

Discussion

Diffusion spectrum imaging of traumatic coma recovery

Over the past several decades, numerous studies in animal models (Gennarelli et al., 1982; Ommaya and Gennarelli, 1974; Smith et al., 2000) and human patients (Adams et al., 1989; Strich, 1961) have implicated lesions of the ARAS arousal network in the pathogenesis of traumatic coma. Yet, identification of disrupted pathways within the ARAS is not currently part of the standard clinical evaluation for patients with traumatic coma. Despite the direct relevance of ARAS connectivity to disorders of consciousness in general (Kinney and Samuels, 1994; Schiff and Plum, 2000), and to traumatic coma in particular, few studies of human ARAS connectivity have been performed to date — a limitation that is likely attributable to the structural complexity of the ARAS network and the inability to resolve this complexity with current imaging techniques. This critical gap in imaging capabilities is a direct hindrance to diagnosis, prognosis, and therapeutic decision-making in patients with traumatic coma. Patients with traumatic brainstem lesions are typically grouped into a single diagnostic and prognostic category that is characterized as “grade 3 diffuse axonal injury” (Adams et al., 1989), without consideration of which specific nodes (i.e. gray matter nuclei) and which specific connections (i.e. white matter pathways) have been disrupted within the ARAS network. Given that recovery of consciousness, communication and functional independence is possible in patients with traumatic coma, even in those with multiple brainstem lesions (Skandsen et al., 2011), it is imperative that imaging techniques are developed to

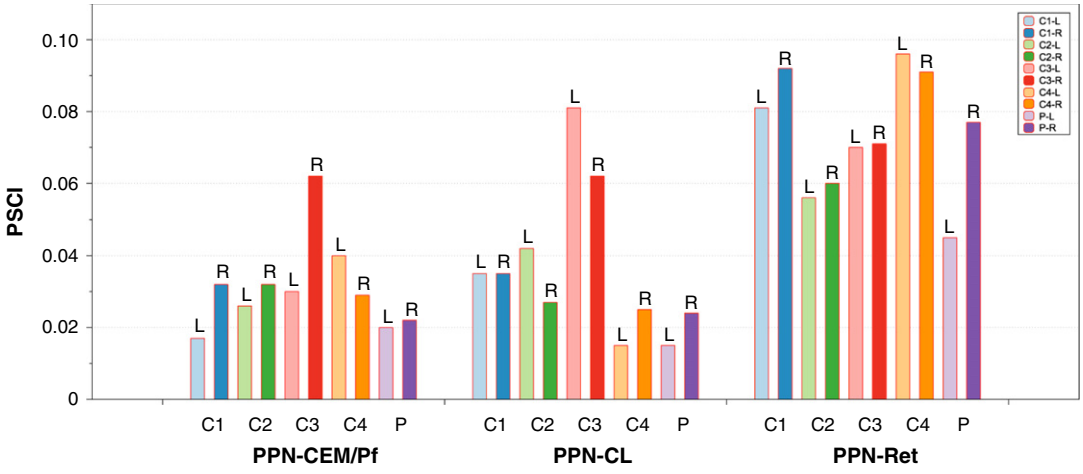

Fig. 3. A comparison of probabilistic streamline connectivity index (PSCI) measurements for the pathways in the four healthy volunteers (C1–C4) and one patient (P) who recovered from traumatic coma. Light colors represent the left hemisphere. Darker colors represent the right hemisphere. The left–right difference for the PPN-Ret pathway in the patient was determined with a t-test to be statistically significantly different from the left–right differences in the controls (p-value = 0.0031). Each pathway was seeded in the pedunculopontine nucleus (PPN). The target ROIs were the following thalamic nuclei: centromedian/parafascicular nucleus (CEM/Pf), central lateral nucleus (CL) and reticular nucleus (Ret).

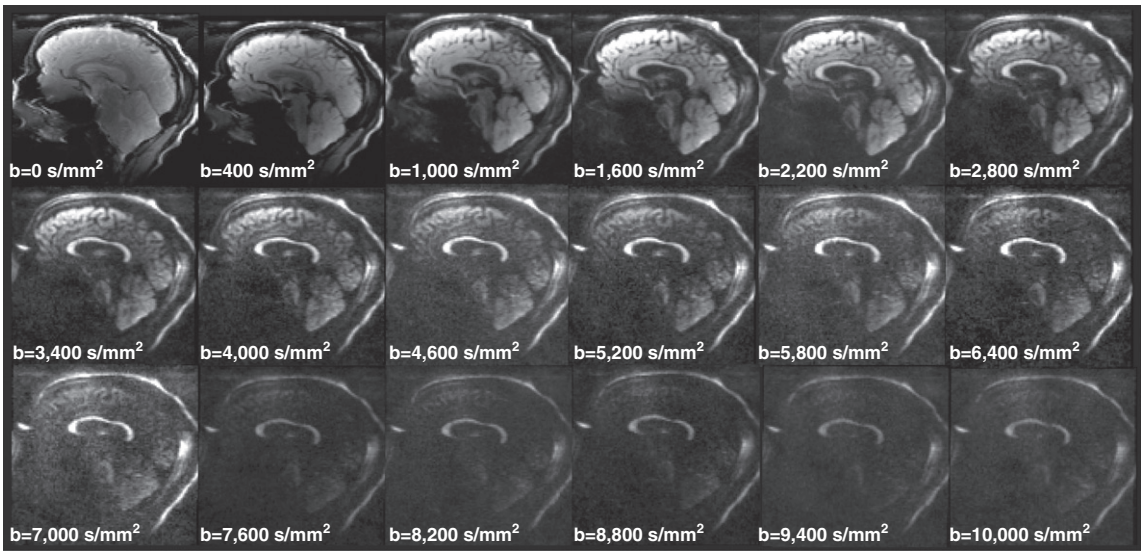

Fig. 4. Sagittal diffusion-weighted images from one healthy volunteer demonstrate the quality of images used in the AxCaliber analysis. Here we show 18 different b-values, all acquired with $\delta = 8.7$ ms and $\Delta = 44$ ms. Each image represents 12 averages and the echo time was matched across all b-values.

map the connectivity of this arousal network and identify patterns of connectivity that predict long-term outcomes. Furthermore, the recent development of pharmacologic and electrophysiologic (i.e. deep brain stimulation) therapies for promoting recovery of consciousness after traumatic coma (Giacino et al., 2012; Schiff et al., 2007; Whyte and Myers, 2009) suggests that ARAS connectivity mapping could be used to select patients for targeted therapies aimed at activating or replacing injured circuits within the network.

At the present time, the optimal imaging acquisition and analysis methods for mapping the structural connectivity of the human ARAS are unknown, and the field of ARAS connectomics is in its infancy. Our initial observations with connectome scanner imaging of the ARAS suggest that the connectome's 300 mT/m gradients are an excellent platform that can be used in future studies to elucidate the connectivity of brainstem networks that subserve human consciousness. Indeed connectivity between the PPN and the intralaminar and reticular nuclei of the thalamus was identified by the MGH–UCLA connectome scanner data not only in healthy human controls (in a pattern that was consistent with prior animal labeling studies; Reese et al., 1995), but PPN-thalamic connectivity was also identified in a 27-year-old man with a near-complete recovery from traumatic coma. The presence of these connections in the patient, as indicated by the PSCI measurements, suggests that traumatic brainstem hemorrhages may cause only partial disruption of the white matter pathways and not complete destruction of ARAS circuitry. We note that axonal injury is not the only pathophysiological mechanism that may cause disruption of fiber tracts as measured by tractography. However, one benefit of studying a patient many years post-injury is that some of the acute pathophysiologic processes that can confound the tractography results, such as edema, are unlikely to be present. Another potential limitation of the tractography results presented here is that we used the ball and two stick model with DSI data, which has the potential for overfitting and creating false positive tracts (Jbabdi et al., 2012).

In this small study (4 healthy subjects and 1 patient), the generalizability of the results is inherently limited. However, our observation that the structural connectivity of key pathways within the human ARAS can be mapped in vivo and robustly reproduced in four subjects is a new and significant finding. Prior work by Edlow et al. (2012) reconstructed human ARAS network pathways in two ex vivo datasets and one in vivo dataset, but the in vivo dataset was not nearly as compelling as the in vivo tractography presented here and to our knowledge these connectivity findings have not been reproduced in multiple subjects or with probabilistic tractography. Also of note, ARAS connectivity mapping in a patient with traumatic coma has only previously been performed ex vivo (Edlow et al., 2013), not in a living patient who recovered from traumatic coma, much less a patient with such an exceptional recovery. Additionally, we report a significant laterality difference in the pathway between the PPN and the reticular nucleus in the recovered patient compared to the controls $p = 0.001$. This finding is of particular interest since the patient experienced a hemorrhage in part of the left PPN but not in the right PPN.

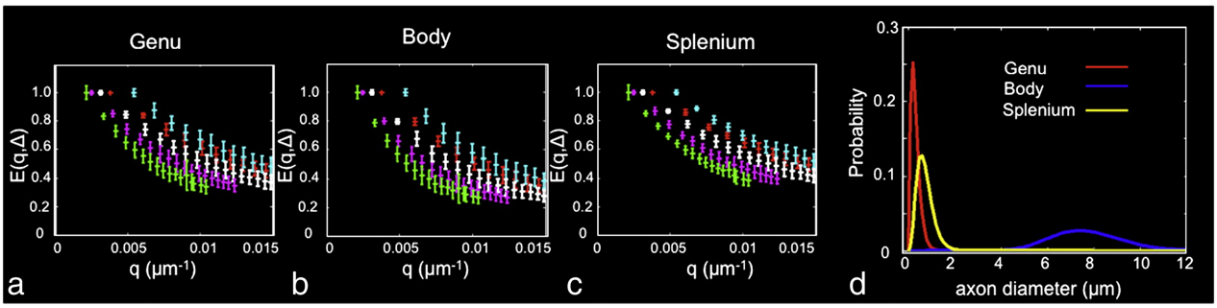

Fig. 5. Mean (n = 4) signal decay curves for ROIs drawn in the a) genu, b) body and c) splenium of the corpus callosum. Green, magenta, white, red and blue curves represent 120 ms, 84 ms, 54 ms, 44 ms and 35 ms diffusion times. Error bars represent the standard deviation across 4 subjects. d) Axon diameter distributions for the genu (red), body (blue) and splenium (yellow) found from the data shown in a), b) and c).

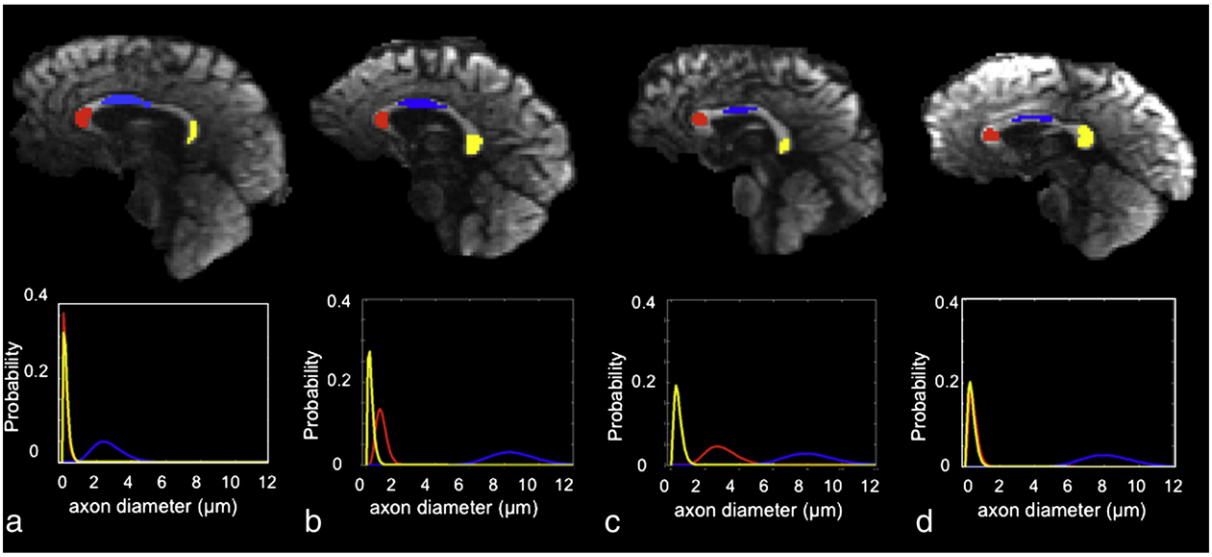

Fig. 6. a–d) ROI delineation (top) and axon diameter distributions (bottom) for subjects 1–4.

However, the variability in the left versus right PPN pathways among the controls (Fig. 2) is significant and therefore further studies are needed to determine the normal range of PSCI values in specific ARAS pathways as well as those values that are consistent with recovery of consciousness. By using the quantitative approach to studying ARAS connectomics proposed here, and by expanding the connectivity analysis beyond the PPN to the many additional ARAS pathways that are critical to arousal (Parvizi and Damasio, 2001), it may ultimately be possible to determine which components of the ARAS network are necessary and sufficient for recovery of arousal, and hence consciousness, after traumatic coma.

Axon diameter mapping in the in vivo human brain

The corpus callosum provides an ideal testing bed for microstructural measures due to the well-established differences in axon diameter and density at different points along its length (A–P) at the midline. Moreover the corpus callosum has the important role of mediating inter-hemispheric connectivity that supports a broad range of cognitive functions. The in vivo human q-space diffusion MRI estimates of axon diameter distributions using the MGH–UCLA connectome scanner are in excellent correspondence with literature, not only at the group and ROI level but also on a pixel-wise basis. Specifically, we see smaller diameter axons at the genu and splenium (~0.5 μm) and larger diameter axons at the body (~8 μm) and this result is consistent across all four subjects. Although our estimated axon diameter distributions provide evidence of axon diameters that are <2 μm, it is unlikely, even with 300 mT/m gradients, that we have sufficient spin-displacement resolution to discriminate between axon diameters that are less than 2 μm (Dyrby et al., 2012).

Future work will aim to test the effects of potential confounds such as brain pulsation, partial volume effects and orientation discrepancies by implementing cardiac gating, higher spatial resolution and models that consider orientational variation. Finally, we aim to compare the effect of gradient strength on the axon diameter estimates in order to help inform protocol development for clinical gradient strengths. We note that extracting the full benefit from the 300 mT/m gradients for quantitative axon diameter measurement requires the system to be stable and linear over the range of gradient strengths used. Along these lines we wish to highlight that the 300 mT/m system has proved exceptionally temporally stable, allowing for example, the lengthy (i.e. 24 h) ex vivo dataset acquired for this manuscript (Figs. 8d, f). The thermal heat removal is sufficient to allow the maximum gradient strength to be used for hours at maximum slices per second of TR and minimum TE. The linearity of the system is 5% over a 20 cm sphere. This is a poorer linearity than typical whole-body gradients but does not have the steep linearity fall-off seen in dedicated head gradients. Although we do a standard position-dependent b-value correction for tractography, we have not assessed the effect of the gradient linearity on the AxCaliber technique. Fortunately, since the corpus callosum is near the isocenter, this is unlikely to be a major problem. Although we were not able to perform any direct validation in this study, we wish to highlight prior studies that have validated the AxCaliber technique in vitro (Assaf et al., 2008) and in animal models (Barazany et al., 2009).

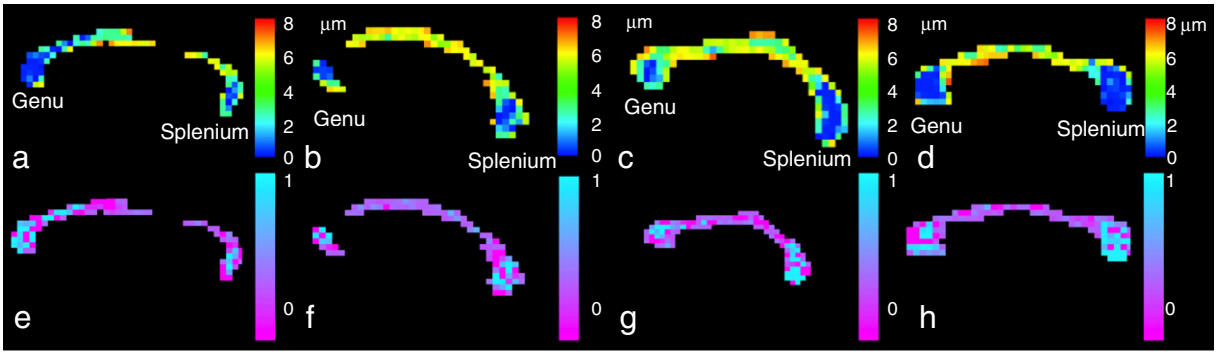

Fig. 7. Pixel-wise estimates in the corpus callosum of subjects 1–4 (left-to-right) for axon diameter (a–d) and axonal density (e–h). The pixel-wise axon diameter value represents the peak of the estimated gamma distribution. The axonal density represents the restricted fraction (fr) estimated in the AxCaliber signal model.

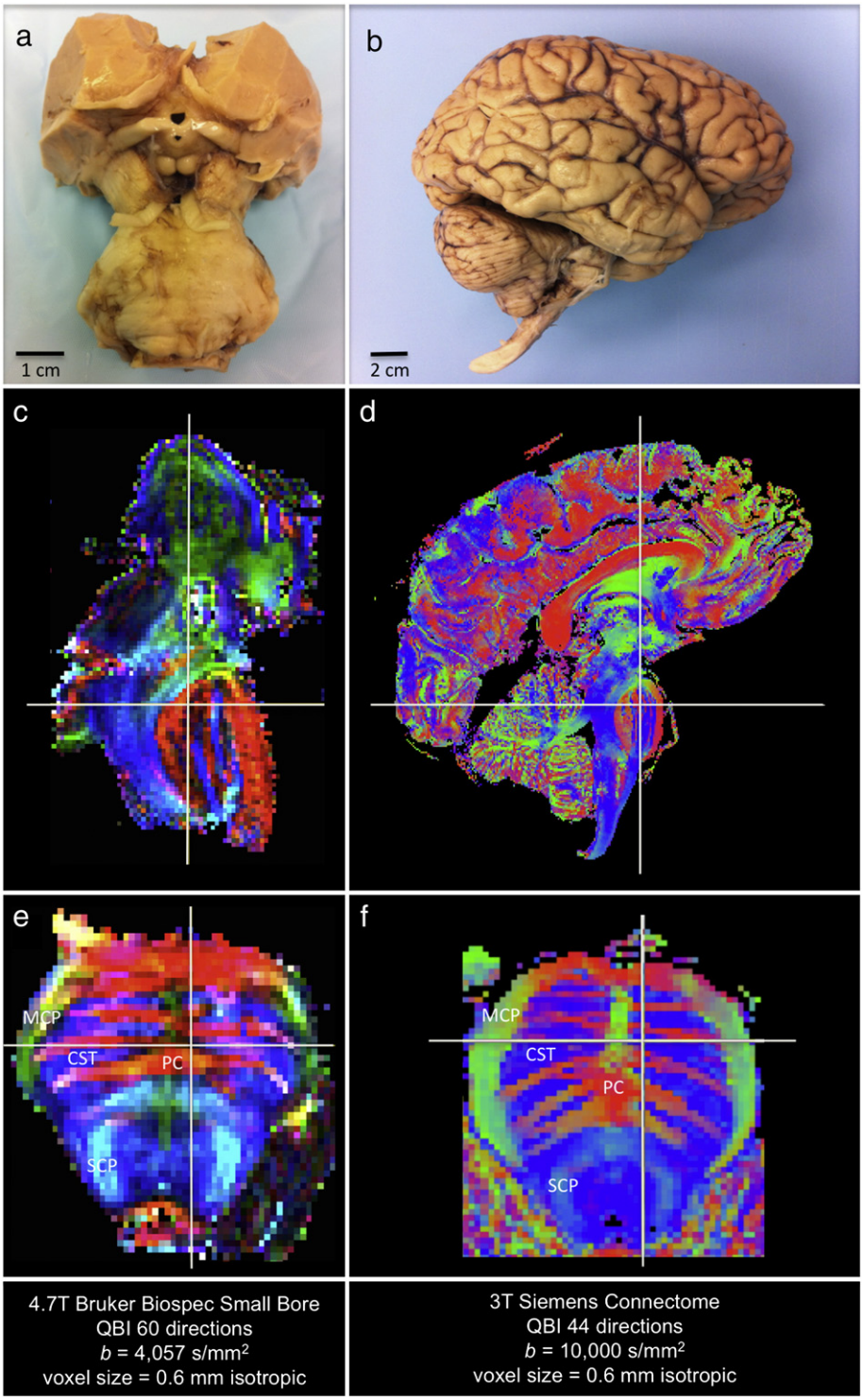

Fig. 8. Ex vivo diffusion imaging of the human brainstem; a) ventral view of a dissected brainstem–diencephalon specimen (consisting of pons, midbrain, thalamus, hypothalamus, and basal forebrain) from a 53-year-old woman who died of non-neurological causes. b) Right lateral view of a whole-brain specimen from a 58-year-old woman who died of non-neurological causes. c) Sagittal view of the directionally-encoded color (DEC) map for the specimen in a). d) Sagittal view of the DEC map for the specimen in b). e) Axial view of the DEC map for the specimen in a) at the level of the rostral pons. f) Axial view of the DEC map for the specimen in b) at the level of the rostral pons. The crosshairs are located in the same voxel in c) and e), as well as in d) and f). The diffusion sequence parameters that were used in each analysis are summarized at the bottom of the figure. The connectome analysis of a whole-brain specimen provides equal spatial resolution (0.6 mm isotropic) and superior angular resolution (i.e. higher b value with similar number of diffusion directions), without sacrificing the signal-to-noise properties and without having to dissect a brain specimen for scanning on a small-bore scanner. Neuroanatomic landmarks: CST, corticospinal tract; MCP, middle cerebellar peduncle; PC, pontine crossing fibers; SCP, superior cerebellar peduncle.

High-resolution (0.6 mm isotropic) q-ball imaging in fixed human brain

High-resolution diffusion imaging of the human brain at autopsy has significant potential as an adjunct to conventional neuropathology. Given the shortened T_2 relaxation time and smaller apparent diffusivity of fixed tissues, the strong gradients of the MGH–UCLA connectome scanner offer even greater benefits to fixed tissue imaging than to in vivo imaging.

A comparison of the directionally-encoded color maps from a whole-brain specimen scanned on the MGH–UCLA connectome

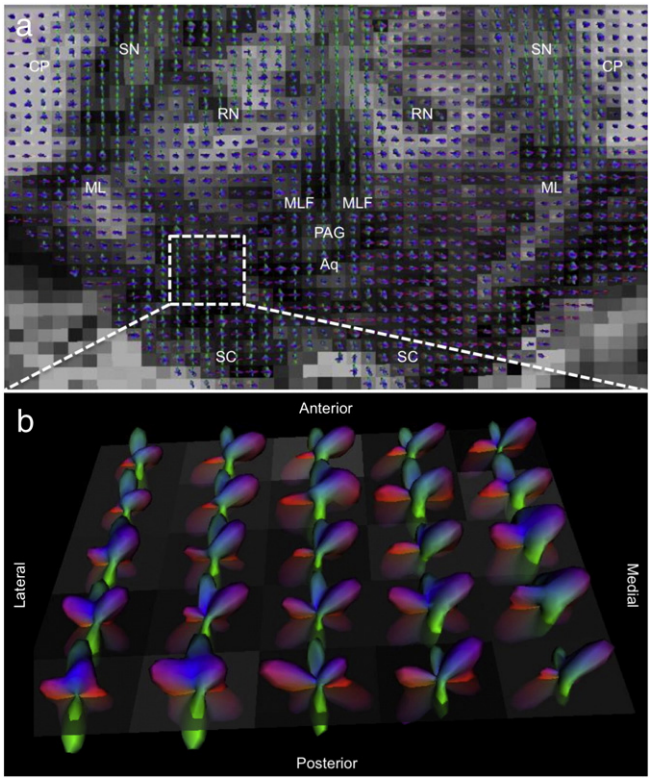

Fig. 9. Orientation distribution function (ODF) analysis of voxels within the cuneiform/subcuneiform nucleus (CSC; mesencephalic reticular formation) in the dorsolateral aspect of the rostral midbrain. (a) The CSC region of interest is outlined on an axial gray-scale fractional anisotropy map. (b) Zoomed view of ODFs within the 5 × 5 voxel CSC region of interest. Voxel size is 0.6 mm in each plane, and the ODFs are color-coded according to the direction of diffusion: blue, superior–inferior; red, medial–lateral; green, anterior–posterior. The ODFs reveal at least three different directional vectors of water diffusion within the CSC. Although the precise neuroanatomic trajectories and targets of each vector cannot be definitively determined, known connectivity from animal and human studies suggests that the blue superior–inferior pathways are ascending to the thalamus via the medial and lateral dorsal tegmental tracts (DTT_M and DTT_L), the green anterior–posterior pathways are projecting ventrally to the hypothalamus via the caudal ventral tegmental tract (VTT_C), and the red medial–lateral pathways are projecting across the posterior commissure to the contralateral midbrain tegmentum. Nomenclature and patterns of connectivity for DTT_M, DTT_L, and VTT_C were first proposed by Shute and Lewis in rats (Shute and Lewis, 1963) and recently refined by Edlow et al. in the human brain (Edlow et al., 2012). Neuroanatomic landmarks: Aq, cerebral aqueduct; CP, cerebral peduncle; ML, medial lemniscus; MLF, medial longitudinal fasciculus; PAG, periaqueductal gray matter; RN, red nucleus; SC, superior colliculus; SN, substantia nigra.

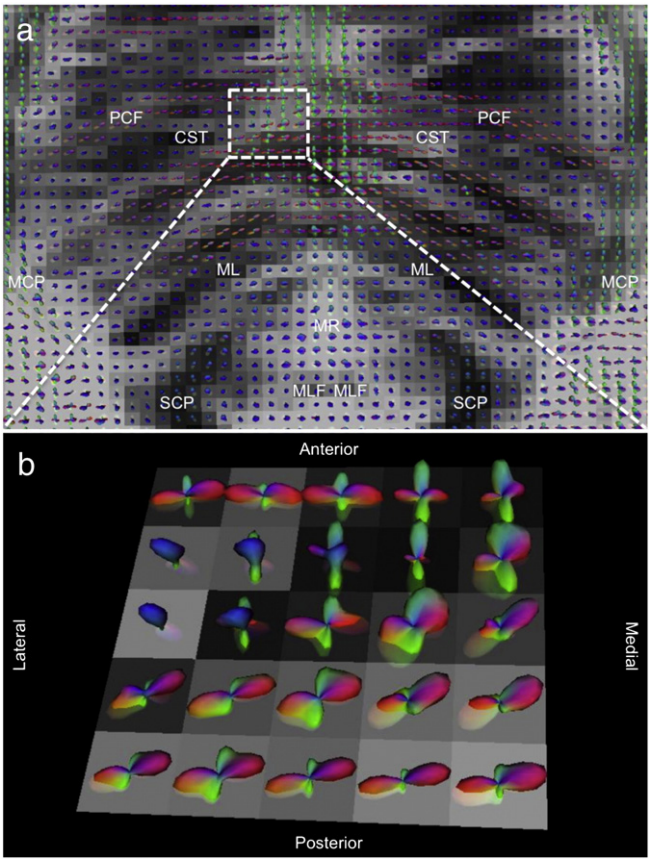

Fig. 10. Orientation distribution function (ODF) analysis of voxels within the basis pontis of the brainstem. (a) A 5 × 5 voxel region of interest is outlined on an axial non-diffusion-weighted (b0) image at the level of the rostral pons. (b) Zoomed view of ODFs within the basis pontis region of interest. Voxel size is 0.6 mm in each plane, and the ODFs are color-coded according to the direction of diffusion: blue, superior–inferior; red, medial–lateral; green, anterior–posterior. The ODFs reveal multiple directional vectors of water diffusion within the basis pontis. Although the precise neuroanatomic trajectories and targets of each vector cannot be definitively determined, known connectivity from animal and human studies suggests that the blue superior–inferior pathways are ascending fibers of the corticospinal tracts (CST) and the red medial–lateral pathways are pontocerebellar crossing fibers (PCF). The green anterior-posterior pathways are of uncertain connectivity. Neuroanatomic landmarks: MCP, middle cerebellar peduncle; ML, medial lemniscus; MLF, medial longitudinal fasciculus; SCP, superior cerebellar peduncle.

scanner and from a dissected brainstem-diencephalon specimen scanned on a small-bore MRI scanner demonstrates that the MGH–UCLA connectome scanner can achieve better resolution of complex crossing fiber pathways in the human brainstem without having to perform a dissection or a small-bore scan. Although the duration of the postmortem scan on the MGH–UCLA connectome scanner was more than 24 h, the time and expense that were saved by eliminating the need for an intricate brain dissection and a separate brainstem-diencephalon scan were substantial. The MGH–UCLA connectome scanner expands neuroimaging capabilities to study axonal connections within multiple brain networks simultaneously in three-dimensions. This methodological advance is expected to be critical for defining cortical and sub-cortical disconnection syndromes that are implicated in the pathogenesis of neurological diseases affecting multiple domains of cognition (Edlow et al., 2013; Geschwind, 1965; Schmahmann and Pandya, 2008).

Furthermore, our ODF analyses of the cuneiform/subcuneiform nucleus (i.e. mesencephalic reticular formation) and basis pontis highlight the ability of the connectome scanner's 300 mT/m gradients to achieve a high degree of angular diffusion resolution without compromising spatial resolution. While multidirectional ODFs and crossing fibers within the basis pontis have previously been demonstrated by other groups (Aggarwal et al., 2013; Tournier et al., 2004), the detection of multidirectional ODFs within the cuneiform/subcuneiform nucleus has not previously been reported, to our knowledge. Indeed, while the neuroanatomic connectivity of the mesencephalic reticular formation has been characterized in animal models over the past several decades with labeling (Kaufman and Rosenquist, 1985; Vertes and Martin, 1988), lesion mapping (Lindsley et al., 1949; Nauta and Kuypers, 1958), and electrophysiologic techniques (Moruzzi and Magoun, 1949; Starzl et al., 1951; Steriade and Glenn, 1982), the connectivity of this critical node in the human ARAS network has yet to be fully elucidated, with current human models of ARAS connectivity based mostly upon extrapolations from animal models. Our ODF results suggest that with the advent of high resolution diffusion tractography of the human brainstem using 300 mT/m gradients, mapping the connectomics of the human ARAS may now be within reach. Moreover, previous methodological limitations in neuroanatomic labeling of postmortem human brain tissue may be overcome by the newly described CLARITY technique (Chung et al., 2013), suggesting that validation of human ARAS tractography data with gold standard histopathological labeling data may soon be possible.

As future studies continue to explore the integration of postmortem diffusion tractography with histopathological analysis, we anticipate that diffusion tractography methods will be refined to achieve greater accuracy and sensitivity. Current tractography methods are plagued by significant levels of false positive and false negative findings (Jones et al., 2013). The correlation of diffusion tractography with histology is critical to validating diffusion tractography methods such that they may ultimately contribute to the clinical evaluation of human neuropathology.

Summary

At the present time the MGH–UCLA connectome scanner is the only one of its kind in the world. However, there are a growing number of research systems with stronger magnetic gradients. The results reported here suggest that these stronger gradients have the potential to provide unprecedented neuroanatomic resolution. Moreover, the benefits of stronger gradients transcend the Human Connectome Project, enabling a much sought-after platform for diffusion imaging methods such as AxCaliber to be applied in the in vivo human brain. The MGH–UCLA connectome scanner's 300 mT/m gradients may thus influence the gradient design for the next generation of MRI scanners. Just as the Human Genome Project generated both basic science knowledge and a broad range of clinical applications, we anticipate that the MGH–UCLA connectome scanner's 300 mT/m gradients will lead to significant breakthroughs in both neuroscience and the clinical care of patients with brain injuries.

Acknowledgments

This work was funded by: a CIHR Fellowship and an NIH Blueprint for Neuroscience Research Grant: U01MH093765, as well as NIH funding from NCRR P41RR14075, NIBIB RO1EB006847 and NINDS R25NS065743 and the Center for Integration of Medicine and Innovative Technology (Boston, MA). We are grateful to the patient who volunteered for this study and whose recovery from traumatic coma continues to inspire this work. Thank you to Louis Vinke for assistance with processing postmortem brain specimens. Thank you to Emi Takahashi and Guangping Dai for assistance with acquisition of brainstem–diencephalon postmortem data acquired on the small-bore scanner.

Conflict of interest

Jennifer McNab has no actual or potential conflicts of interest.
Brian Edlow has no actual or potential conflicts of interest.
Thomas Witzel has no actual or potential conflicts of interest.
Susie Huang has no actual or potential conflicts of interest.
Lawrence Wald has no actual or potential conflicts of interest.
Hannah Kinney has no actual or potential conflicts of interest.
Rebecca Folkerth has no actual or potential conflicts of interest.
Dylan Tisdall has no actual or potential conflicts of interest.
Julien Cohed-Adad has no actual or potential conflicts of interest.
Boris Keil has no actual or potential conflicts of interest.

Himanshu Bhat has a potential conflict of interest. He is an employee of Siemens Medical Solutions, USA Inc.

Thorsten Feiweier has three potential conflicts of interest: He is an employee of Siemens AG. He is owning stocks of Siemens AG. He is holding patents filed by Siemens AG.

Kecheng Liu has a potential conflict of interest. He is an employee of Siemens Medical Solutions, USA Inc.

Keith Heberlein has a potential conflict of interest. He is an employee of Siemens Medical Solutions, USA Inc. He holds shares of stock in the parent company Siemens AG.

References

Aboitiz, F., Scheibel, A.B., Fisher, R.S., Zaidel, E., 1992. Fiber composition of the human corpus callosum. Brain Res. 598, 143–153.
Adams, J.H., Doyle, D., Ford, I., Gennarelli, T.A., Graham, D.I., McLellan, D.R., 1989. Diffuse axonal injury in head injury: definition, diagnosis and grading. Histopathology 15, 49–59.
Aggarwal, M., Zhang, J., Pletnikov, O., Crain, B., Troncoso, J., Mori, S., 2013. Feasibility of creating a high-resolution 3D diffusion tensor imaging based atlas of the human brainstem: a case study at 11.7 T. NeuroImage 74, 117–127.
Alexander, D.C., Hubbard, P.L., Hall, M.G., Moore, E.A., Ptito, M., Parker, G.J.M., Dyrby, T.B., 2010. Orientationally invariant indices of axon diameter and density from diffusion MRI. NeuroImage 52, 1374–1389.
Anwander, A., Pampel, A., Knosche, T.R., 2010. In vivo measurement of cortical anisotropy by diffusion-weighted imaging correlates with cortex type. Proc. Int. Soc. Magn. Reson. Med. 18, 109.
Assaf, Y., Blumenfeld-Katzir, T., Yovel, Y., Basser, P.J., 2008. AxCaliber: a method for measuring axon diameter distribution from diffusion MRI. Magn. Reson. Med. 59, 1347–1354.
Barazany, D., Basser, P.J., Assaf, Y., 2009. In vivo measurement of axon diameter distribution in the corpus callosum of rat brain. Brain 132, 1210–1220.
Behrens, T.E.J., Woolrich, M.W., Jenkinson, M., Johansen-Berg, H., Nunes, R.G., Clare, S., Matthews, P.M., Brady, J.M., Smith, S.M., 2003. Characterization and propagation of uncertainty in diffusion-weighted MR imaging. Magn. Reson. Med. 50, 1077–1088.
Bell, R.S., Vo, A.H., Neal, C.J., Tigno, J., Roberts, R., Mossop, C., Dunne, J.R., Armonda, R.A., 2009. Military traumatic brain and spinal column injury: a 5-year study of the impact blast and other military grade weaponry on the central nervous system. J. Trauma 66, S104–S111.
Bodammer, N., Kaufmann, J., Kanowski, M., Tempelmann, C., 2004. Eddy current correction in diffusion-weighted imaging using pairs of images acquired with opposite diffusion gradient polarity. Magn. Reson. Med. 51, 188–193.
Bruns, J., Hauser, W.A., 2003. The epidemiology of traumatic brain injury: a review. Epilepsia 44, 2–10.
Callaghan, P.T., 1991. Principles of Nuclear Magnetic Resonance Microscopy. Oxford University Press.
Callaghan, P.T., Eccles, C.D., Xia, Y., 1988. NMR microscopy of dynamic displacements — k-space and q-space imaging. J. Phys. E: Sci. Instrum. 21, 820–822.
Chung, K., Wallace, J., Kim, S.Y., Kalyanasundaram, S., Andalman, A.S., Davidson, T.J., Mirzabekov, J.J., Zalocusky, K.A., Mattis, J., Denisin, A.K., Pak, S., Berstein, H., Ramakrishnan, C., Grosenick, L., Gradinaru, V., Deisseroth, K., 2013. Structural and molecular interrogation of intact biological systems. Nature. http://dx.doi.org/10.1038/nature12107.
Cluskey, S., Ramsden, D.B., 2001. Mechanisms of neurodegeneration in amyotrophic lateral sclerosis. Mol. Pathol. 54, 386–392.
Cory, D.G., Garroway, A.N., 1990. Measurement of translational displacement probabilities by NMR—an indicator of compartmentation. Magn. Reson. Med. 14, 435–444.
D'Arceuil, H.E., Westmoreland, S., de Crespigny, A.J., 2007. An approach to high resolution diffusion tensor imaging in fixed primate brain. NeuroImage 35, 553–565.
DuBose, J.J., Barmparas, G., Inaba, K., Stein, D.M., Scalea, T., Cancio, L.C., Cole, J., Eastridge, B., Blackboune, L., 2011. Isolated severe traumatic brain injuries sustained during combat operations: demographics, mortality outcomes, and lessons to be learned from contrasts to civilian counterparts. J. Trauma 70, 11–16.
Dyrby, T.B., Sogaard, L.V., Hall, M.G., Ptito, M., Alexander, D.C., 2012. Contrast and stability of the axon diameter index from microstructure imaging with diffusion MRI. Magn. Reson. Med. http://dx.doi.org/10.1002/mrm.24501.
Edlow, B., Takahashi, E., Wu, O., Benner, T., Dai, G., Bu, L., Grant, P.E., Greer, D.M., Greenberg, S.M., Kinney, H.C., Folkerth, R.D., 2012. Neuroanatomic connectivity of the human ascending arousal system critical to consciousness and its disorders. J. Neuropathol. Exp. Neurol. 71, 531–546.
Edlow, B.L., Haynes, R.L., Takahashi, E., Klein, J.P., Cummings, P., Benner, T., Greer, D.M., Greenberg, S.M., Wu, O., Kinney, H.C., Folkerth, R.D., 2013. Disconnection of the ascending arousal system in traumatic coma. J. Neuropathol. Exp. Neurol. 72, 505–523.
Faul, M., Xu, L., Wald, M.M., Coronado, V.G., 2010. Traumatic Brain Injury in the United States: Emergency Department Visits, Hospitalizations, and Deaths. Center for Disease Control and Prevention, National Center for Injury Prevention and Control.
Fernandez-Espejo, D., Soddu, A., Cruse, D., Palacios, E.M., Junque, C., Vanhaudenhuyse, Rivas, E., Newcombe, V., Menon, D.K., Pickard, J.D., Laureys, S., Owen, A.M., 2012. A role for the default mode network in the bases of disorders of consciousness. Ann. Neurol. 72, 335–343.
Fuller, P., Sherman, D., Pedersen, N.P., Saper, C.B., L, J, 2011. Reassessment of the structural basis of the ascending arousal system. J. Comp. Neurol. 519, 933–956.
Gennarelli, T.A., Thibault, L.E., Adams, J.H., Graham, D.I., Thompson, C.J., Marcincin, R.P., 1982. Diffuse axonal injury and traumatic coma in the primate. Ann. Neurol. 12, 564–574.
Geschwind, N., 1965. Disconnexion syndromes in animals and man. I. Brain 88, 237–294.
Giacino, J.T., Whyte, J., Bagiella, E., Kalmar, K., Childs, N., Khademi, A., Eifert, B., Long, D., Katz, D.I., Cho, S., Yablon, S.A., Luther, M., Hammond, F.M., Nordenbo, A., Novak, P., Mercer, W., Maurer-Karattup, P., Sherer, M., 2012. Placebo-controlled trial of amantadine for severe traumatic brain injury. N. Engl. J. Med. 366, 819–826.
Heads, T., Pollock, M., Robertson, A., Sutherland, W.H., Allpress, S., 1991. Sensory nerve pathology in amyotrophic lateral sclerosis. Acta Neuropathol. Berl. 82, 316–320.
Heidemann, R.M., Porter, D.A., Anwander, A., Feiweier, T., Heberlein, K., Knösche, T.R., Turner, R., 2010. Diffusion imaging in humans at 7 T using readout-segmented EPI and GRAPPA. Magn. Reson. Med. 64, 9–14.
Hess, C.P., Muherjee, P., Han, E.T., Xu, D., Vigneron, D.B., 2006. Q-ball reconstruction of multimodal fiber orientations using the spherical harmonic basis. Magn. Reson. Med. 56, 104–117.

Hoffmeister, B., Janig, W., Lisney, S.J., 1991. A proposed relationship between circumference and conduction velocity of unmyelinated axons from normal and regenerated cat hindlimb cutaneous nerves. Neuroscience 42, 603–611.
Horowitz, A., Barazany, D., Yovel, G., Assaf, Y., 2012. Inter hemispheric transfer time and axon diameter properties of the corpus callosum. Proc. Int. Soc. Magn. Reson. Med. 3619.
Hursh, J.B., 1939. The properties of growing nerve fibers. Am. J. Physiol. 127, 29–35.
Jbabdi, S., Sotiropoulos, S.N., Savio, A.M., Grana, M., Behrens, T.E.J., 2012. Model-based analysis of multishell diffusion MR data for tractography: how to get over fitting problems. Magn. Reson. Med. 68, 1846–1855.
Jones, D.K., Knösche, T.R., Turner, R., 2013. White matter integrity, fiber count, and other fallacies: the do's and don'ts of diffusion MRI. Magn. Reson. Med. 73, 239–254.
Kaufman, E.S., Rosenquist, A.C., 1985. Afferent connections of the thalamic intralaminar nuclei in the cat. Brain Res. 335, 281–296.
Keil, B., Blau, J.N., Biber, S., Hoecht, P., Tountcheva, V., Setsompop, K., Triantafyllou, C., Wald, L.L., 2012. A 64-channel 3 T array coil for accelerated brain MRI. Magn. Reson. Med. http://dx.doi.org/10.1002/mrm.24427.
Kinney, H.C., Samuels, M.A., 1994. Neuropathology of the persistent vegetative state. A review. J. Neuropathol. Exp. Neurol. 53, 548–558.
Kinomura, S., Larsson, J., Gulyas, B., Roland, P.E., 1996. Activation by attention of the human reticular formation and thalamic intralaminar nuclei. Science 271, 512–515.
Leuze, C.W., Anwander, A., Bazin, P.L., Stüber, C., Reimann, K., Geyer, S., Turner, R., 2012. Layer-specific intracortical connectivity revealed with diffusion MRI. Cereb. Cortex. http://dx.doi.org/10.1093/cercor/bhs311.
Lindsley, D.B., Bowden, J.W., Magoun, H.W., 1949. Effect upon the EEG of acute injury to the brain stem activating system. Electroencephalogr. Clin. Neurophysiol. 1, 475–486.
Mai, J.K., Paxinos, G., Voss, T., 2008. Atlas of the Human Brain. Elsevier.
Marner, L., Nyengaard, J.R., Tang, Y., Pakkenberg, B., 2003. Marked loss of myelinated nerve fibers in the human brain with age. J. Comp. Neurol. 462, 144–152.
McNab, J.A., Jbabdi, S., Deoni, S.C.L., Douaud, G., Behrens, T.E.J., Miller, K.L., 2009. High resolution diffusion weighted imaging in fixed human brain using diffusion weighted steady state free precession. NeuroImage 46, 775–785.
McNab, J.A., Polimeni, J.R., Wang, R., Augustinack, J.C., Fujimoto, K., Stevens, A., Janssens, T., Farivar, R., Folkerth, R.D., Vanduffel, W., Wald, L.L., 2013. Surface based analysis of diffusion orientation for identifying architectonic domains in the in vivo human cortex. NeuroImage 69, 87–100.
Miller, K.L., Stagg, C.J., Douaud, G., Jbabdi, S., Smith, S.M., Behrens, T.E.J., Jenkinson, M., Chance, S.A., Esiri, M.M., Voets, N.L., Jenkinson, N., Aziz, T.Z., Turner, M.R., Johansen-Berg, H., McNab, J.A., 2011. Diffusion imaging of whole, post-mortem human brains on a clinical MRI scanner. NeuroImage 57, 167–181.
Morel, A., Magnin, M., Jeanmonod, D., 1997. Multiarchitectonic and stereotactic atlas of the human thalamus. J. Comp. Neurol. 387, 588–630.
Moruzzi, P., Magoun, H.W., 1949. Brain stem reticular formation and activation of the EEG. Electroencephalogr. Clin. Neurophysiol. 1, 455–473.
Nauta, W.J.H., Kuypers, H.G.J.M., 1958. Some ascending pathways in the brain stem reticular formation. In: Jasper, H.H., Proctor, L.D., Knighton, R.S., Noshay, W.C., Costello, R.T. (Eds.), Reticular Formation of the Brain. Little, Brown, and Company, Boston, MA, pp. 3–30.
Ommaya, A.K., Gennarelli, T.A., 1974. Cerebral concussion and traumatic unconsciousness. Correlation of experimental and clinical observations of blunt head injuries. Brain 97, 633–654.
Ong, H.H., Wehrli, F.W., 2010. Quantifying axon diameter and intra-cellular volume fraction in excised mouse spinal cord with q-space imaging. NeuroImage 51, 1360–1366.
Parvizi, P.J., Damasio, A., 2001. Consciousness and the brainstem. Cognition 79, 135–160.
Parvizi, J., Damasio, A.R., 2003. Neuroanatomical correlates of brainstem coma. Brain 126, 1524–1536.
Paxinos, G., Xu-Feng, H., Sengul, G., Watson, C., 2011. Organization of Brainstem Nuclei. The Human Nervous System. Elsevier, Amsterdam.
Piven, J., Bailey, J., Ranson, B.J., Arndt, S., 1997. An MRI study of the corpus callosum in autism. Am. J. Psychiatry 154, 1051–1056.
Reese, N.B., Garcia-Rill, E., Skinner, R.D., 1995. The pedunculopontine nucleus—auditory input, arousal and pathophysiology. Prog. Neurobiol. 47, 105–133.
Ringo, J.L., Doty, R.W., Demeter, S., Simard, P.Y., 1994. Time is of the essence: a conjecture th at hemispheric specialization arises from interhemispheric conduction delay. Cereb. Cortex 4, 331–343.
Schiff, N.D., Plum, F., 2000. The role of arousal and "gating" systems in the neurology of impaired consciousness. J. Clin. Neurophysiol. 17, 438–452.
Schiff, N.D., Giacino, J.T., Kalmar, K., Victor, J.D., Baker, K., Gerber, M., Fritz, B., Eisenberg, B., Biondi, T., O'Connor, J., Kobylarz, E.J., Farris, S., Machado, A., McCagg, C., Plum, F., Fins, J.J., Rezai, A.R., 2007. Behavioural improvements with thalamic stimulation after severe traumatic brain injury. Nature 448, 600–603.
Schmahmann, J.D., Pandya, D.N., 2008. Disconnection syndromes of basal ganglia, thalamus, and cerebrocerebellar systems. Cortex 44, 1037–1066.
Setsompop, K., Kimmlingen, R., Eberlein, E., Witzel, T., Cohen-Adad, J., McNab, J.A., Keil, B., Tisdall, M.D., Hoecht, P., Dietz, P., Cauley, S.F., Tountcheva, V., Matschl, V., Lenz, V.H., Heberlein, K., Potthast, A., Thein, H., Van Horn, J., Toga, A., Schmitt, F., Lehne, D., Rosen, B.R., Wedeen, V., Wald, L.L., 2013. Pushing the limits of *in vivo* diffusion MRI for the Human Connectome Project. Neuroimage 80, 220–233.
Shute, C.C., Lewis, P.R., 1963. Cholinesterase-containing systems of the brain of the rat. Nature 199, 1160–1164.
Silva, S., Alacoque, X., Fourcade, O., Samil, K., Marque, P., Woods, R., Mazziotta, J., Chollet, F., Loubinoux, I., 2010. Wakefulness and loss of awareness: brain and brainstem interaction in the vegetative state. Neurology 74, 313–320.
Skandsen, T., Kvistad, K.A., Solheim, O., Lydersen, S., Strand, I.H., Vik, A., 2011. Prognostic value of magnetic resonance imaging in moderate and severe head injury: a prospective study of early MRI findings and one-year outcome. J. Neurotrauma 28, 691–699.
Smith, D.H., Nonaka, M., Miller, R., Leoni, M., Chen, X.H., Alsop, D., Meaney, D.F., 2000. Immediate coma following inertial brain injury dependent on axonal damage in the brainstem. J. Neurosurg. 93, 315–322.
Stanisz, G.J., Szafer, A., Wright, G.A., Henkelman, R.M., 1997. An analytical model for restricted diffusion in bovine optic nerve. Magn. Reson. Med. 37, 103–111.
Starzl, T.E., Taylor, C.W., Magoun, H.W., 1951. Ascending conduction in reticular activating system, with special reference to the diencephalon. J. Neurophysiol. 14, 461–477.
Steriade, M., Glenn, L.L., 1982. Neocortical and caudate projections of intralaminar thalamic neurons and their synaptic excitation from midbrain reticular core. J. Neurophysiol. 48, 352–371.
Strich, S.J., 1961. Shearing of nerve fibers as a cause of brain damage due to head injury: a pathological study of twenty cases. Lancet 2, 443–448.
Tournier, J.D., Calamante, F., Gadian, D.G., Connelly, A., 2004. Direct estimation of the fiber orientation density function from diffusion-weighted MRI data using spherical deconvolution. NeuroImage 23, 1176–1185.
Van Essen, D.C., Ugurbil, K., Auerbach, E., Barch, D., Behrens, T.E., Bucholz, R., Chang, A., Chen, L., Corbetta, M., Curtiss, S.W., Della Penna, S., Feinberg, D., Glasser, M.F., Harel, N., Heath, A.C., Larson-Prior, L., Marcus, D., Michalareas, G., Moeller, S., Oostenveld, R., Petersen, S.E., Prior, F., Schlaggar, B.L., Smith, S.M., Snyder, A.Z., u, J, Yacoub, WU–Minn HCP Consortium, 2012. The human connectome project: a data acquisition perspective. NeuroImage 62, 2222–22431.
Vanhaudenhuyse, A., Noirhomme, Q., Tshibanda, L.J.-F., Bruno, M.-A., Boveroux, P., Schnakers, C., Soddu, A., Perlbarg, V., 2010. Default network connectivity reflects the level of consciousness in non-communicative brain-damaged patients. Brain 133, 161–171.
Vertes, R.P., Martin, G.F., 1988. Autoradiographic analysis of ascending projections from the pontine and mesencephalic reticular formation and the median raphe nucleus in the rat. J. Comp. Neurol. 275, 511–541.
Wang, R., Benner, T., Sorensen, A.G., Wedeen, V.J., 2007. Diffusion toolkit: a software package for diffusion imaging data processing and tractography. Proc. Int. Soc. Magn. Reson. Med. 15, 3720.
Wedeen, V., Hagmann, P., Tseng, W., Reese, T., Weisskoff, R., 2005. Mapping complex tissue architecture with diffusion spectrum magnetic resonance imaging. Magn. Reson. Med. 54, 1377–1386.
Wedeen, V.J., Wang, R.P., Schmahmann, J.D., Benner, T., Tseng, W.Y.I., Dai, G., Pandya, D.N., Hagmann, P., D'Arceuil, H., de Crespigny, A.J., 2008. Diffusion spectrum magnetic resonance imaging (DSI) tractography of crossing fibers. NeuroImage 41, 1267–1277.
Whyte, J., Myers, R., 2009. Incidence of clinically significant responses to zolpidem among patients with disorders of consciousness. Am. J. Phys. Med. Rehabil. 88, 410–418.
Zhang, H., Hubbard, P.L., Parker, G.J.M., Alexander, D.C., 2011. Axon diameter mapping in the presence of orientation dispersion with diffusion MRI. NeuroImage 56, 1301–1315.